International Journal of Heat and Mass Transfer 52 (2009) 5867–5877

Contents lists available at ScienceDirect

International Journal of Heat and Mass Transfer

journal homepage: www.elsevier.com/locate/ijhmt

Modeling of coaxial powder flow for the laser direct deposition process

S.Y. Wen, Y.C. Shin *, J.Y. Murthy, P.E. Sojka

School of Mechanical Engineering, Purdue University, West Lafayette, IN 47907, USA

A R T I C L E   I N F O

Article history:
Received 4 December 2008
Received in revised form 31 July 2009
Accepted 31 July 2009
Available online 26 September 2009

Keywords:
Laser direct deposition
Coaxial powder flow
Laser heating
Numerical modeling

A B S T R A C T

The supplying powder jet conditions in a direct deposition process greatly influence the quality and property of deposition products. Coaxial powder flow provides the means of precise deposition due to its omnidirectional nature in a direct deposition process. In this paper, a comprehensive numerical model is presented to predict the whole process of coaxial powder flow, including the particle stream flow in and after the nozzle and laser–particle interaction process. By solving the coupled momentum transfer equations between the particle and gas phase while incorporating particle temperature evolution, the dynamic and thermal behavior of multi-particles in the stream is completely modeled. Calculated and measured results are well matched. The model is capable of predicting the powder stream structure and multi-particle phase change process with liquid fraction evolution throughout the entire process while considering the particle morphology and size distribution in real powder samples.

1. Introduction

The laser direct deposition process is used for rapid freeform fabrication of fully dense components with good metallurgical properties. In this process, powder is usually fed into a laser-heated spot to form a melt pool, which solidifies quickly after the laser beam moves away. One of the challenging issues is to understand how the material powder is supplied to the target surface since it influences the particle utilization efficiency, track dimensions, and even the final properties of the product.

Coaxial nozzles, which allow the powder stream to flow coaxially with the laser beam, provide the capability of precise deposition due to omnidirectional nature. Although coaxial powder supply has been popularly used for deposition, comprehensive modeling is still lacking due to the complex physics involved, such as two-phase powder–gas flow and laser–powder interaction.

The coaxial powder flow concentration mode was studied without considering thermal behavior of the particles [1–11]. The importance of the nozzle arrangement and gas flow settings to the powder concentration mode has been revealed through the coaxial powder distribution calculation [1–3]. Pan and Liou [4] numerically studied the metallic powder flow in a coaxial nozzle by considering the effect of non-spherical collision with the nozzle wall and quantitatively predicting the concentration variation of a coaxial gravity-driven powder flow with various powder passage configurations and gas settings [5]. Pinkerton and Li [6–8] proposed a unique mathematical model, which directly relates coaxial powder structure to nozzle dimensions and flow rates. Zekovic et al. [9] presented a computational fluid dynamics method to obtain the multi-phase gas–powder flow structures for radially symmetrical nozzles. The laser attenuation process during coaxial powder flow was also considered by some of earlier studies [2,7,10,11]. However, for a complete model of a coaxial powder flow process, it is also necessary to consider the particle heating process under laser irradiation since it determines the thermal conditions of particles before they reach the melt pool.

A single particle heating process has been separately considered without modeling the powder stream structure [12–14]. A simple melting model based on the energy balance of a particle with given in-flight direction was considered in Ref. [12] to optimize the deposition process. A single spherical particle heating problem has been numerically studied by Lin [13] and further developed by Liu and Lin [14] with consideration of heating, melting and evaporation processes under irradiation of a CO_2 laser beam in a coaxial laser cladding process.

In the studies that considered both powder concentration and laser heating process, some simplifying assumptions about the powder flow were made and its structure was predefined [15–23]. Assuming an average particle radius, powder flow temperature from coaxial nozzles was calculated and also experimentally investigated by Vetter et al. [15] and Pinkerton [16]. Using predefined stream spread and speed for powder particles, an analytical model was presented [17–19] to study the particle temperature distribution in the powder flow and the attenuation of the laser energy distribution. Gaussian powder distribution was assumed by Han et al. [20,21], Qi et al. [22], and He and Mazumder [23] in their direct deposition models for the powder heating process and laser attenuation.

---

* Corresponding author. Tel.: +1 765 494 9775; fax: +1 765 494 0539.
E-mail address: shin@purdue.edu (Y.C. Shin).

0017-9310/$ - see front matter © 2009 Elsevier Ltd. All rights reserved.
doi:10.1016/j.ijheatmasstransfer.2009.07.018

Nomenclature

Latin symbols

a_1, a_2, a_3, a_4	constants
A	area (m^2)
c_p	heat capacity (J/kg/K)
C_D	drag coefficient
C_1, C_2, C_μ	coefficients in turbulent transport equations
d	diameter (m)
$\bar{d}$	particle size constant (m)
D	characteristic width (m)
f	liquid fraction (%)
F	mass fraction (%)
g	gravitational acceleration (m/s^2)
G_k	rate of production of kinetic energy ($kg/m/s^3$)
h	convection coefficient ($W/K/m^2$)
I	laser intensity (W/m^2)
k	kinetic energy of turbulence (m^2/s^2)
L	laser field of depth (m)
L_f	fusion heat (J/kg)
m	mass (kg)
$\dot{m}$	mass flow rate (kg/s)
n	number of particle trajectories
n	spread parameter
Nu	Nusselt number
p	pressure (N/m^2)
r	radial coordinates (m)
R	radius (m)
Re	Reynolds number
P	laser power (W)
Pr	Prandtl number
s	surface area of a sphere having the same volume as the particle (m^2)
S	actual surface area of the particle (m^2)
St	Stokes number
t	time (s)
T	temperature (K)
u	velocity (m/s)
V	volume (m^3)
x	axial coordinates (m)
$\bar{x}$	position vector

Greek symbols

ρ	density (kg/m^3)
τ	response time (s)
θ	angle (°)
γ	ratio of properties
ε	rate of dissipation of turbulence energy (m^2/s^3)
λ	thermal conductivity (W/K/m)
ξ	absorptivity (%)
ϕ	source term ($kg/m^2/s^2$)
φ	shape factor
μ	dynamic viscosity (Pa s)
α	parameter
β	parameter
δ	Flag for different temperature range
$\sigma_k, \sigma_\varepsilon$	coefficients in turbulent transport equations

Subscripts

b	laser beam
C	cell
d	diameter
f	laser focus
i	iteration level
j	number
i,j	direction
l	laminar
l	liquid
liq	liquidus
o	laser output
p	particle
r	radial direction
sol	solidus
t	turbulent
x	axial direction
ρ	density

As seen from the above discussion, the comprehensive modeling that simultaneously considers both dynamic and thermal behaviors of multiple particles distributed in the coaxial powder flow is still lacking. The assumption of standard Gaussian mode may not always be accurate, since it may deviate from Gaussian depending on powder properties, configurations of nozzle, gas settings, and standoff distances. To be more rigorous, in this paper, a comprehensive model is presented to predict the powder flow structure and laser particle heating process in terms of multi-particle behavior, thus revealing the characteristics of powder supply for the coaxial deposition process.

2. Model development

2.1. Background description

A typical coaxial nozzle configuration is characterized by inner, middle, and outer nozzles [1–7]. Driven by the carrier gas or gravity force, the powder of certain material is fed through the middle nozzle. The inner nozzle also provides a passage shared by the laser beam and inner gas that helps prevent the particles from attaching to the laser optics. The middle and outer nozzles together provide a passage for the outer gas used for shielding. However, there is another novel type of coaxial nozzle that does not use outer gas. The coaxial powder flow with this nozzle (Precitec YC50), used in the present study, is schematically illustrated in Fig. 1, which shows the cross-section of the conical shape nozzle. The blue lines represent the outer nozzle contour, while the green lines represent the inner one.[1]

In the deposition process, the powder, whose feed rate is precisely controlled by a powder feeder, is uniformly fed into the conical channel via a powder distributor in the supply path. After passing through the nozzle, the particles will travel through the laser irradiation zone (Nd:YAG laser in this study), in which the particles will be rapidly heated up as illustrated in Fig. 1. The goal of this study is to conduct a numerical study to reveal the complex and detailed phenomena of powder–gas two phase flows within and below the nozzle and the associated laser–particle interaction process.

2.2. Calculation domain

Fig. 2 describes the calculation domain used in the numerical model. Due to the assumption of uniform powder flow at the inlet, the calculation domain in Fig. 2 displays a radial 2D slice of the 3D domain with the center line as the axisymmetric axis. The powder

---

[1] For interpretation of the references to color in text, the reader is referred to the web version of this paper.

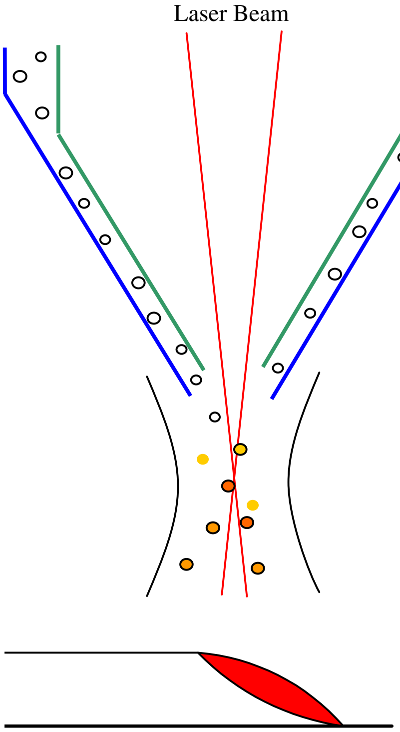

Fig. 1. Illustration of coaxial powder flow.

passage, which is formed by the inner and outer nozzle, has a center diameter of 57.47 mm at inlet and 10.34 mm at outlet. The powder passage width changes from 3.47 mm at inlet to 1.2 mm at outlet. The heights of the passage walls are 55.00 mm and 56.00 mm, respectively. The ambient space below the nozzle is chosen to be 50 × 100 mm^2, which is large enough to make the boundaries not affected by the powder stream. The origin point is located at the center point of the bottom tip circle of the inner nozzle, with the positive x-axis in downward direction and r-axis in outward direction.

2.3. Solution technique

As discussed above, the gas–powder flow with laser–powder interaction is a complex two phase problem. In this paper, the gas phase is treated as continuum, while the particle flow is simulated as a discrete phase that consists of particles dispersed in the continuum phase. The behavior of continuous gas phase is modeled by solving the time-averaged Navier–Stokes equations, while the dispersed phase is solved in a Lagrangian frame of reference by tracking a certain number of particles through the calculated flow field. The coupling between these two phases will be seen from the governing equations in Section 2.4.1. The coupling is accomplished by alternatively solving the continuous and discrete equations (in Section 2.4.2) until the convergence for both phases. While powders flow through the gas, they interact with the laser beam. A unique user defined function described in Section 2.4.3 is incorporated to solve the thermal behavior of the particle phase as calculation continues.

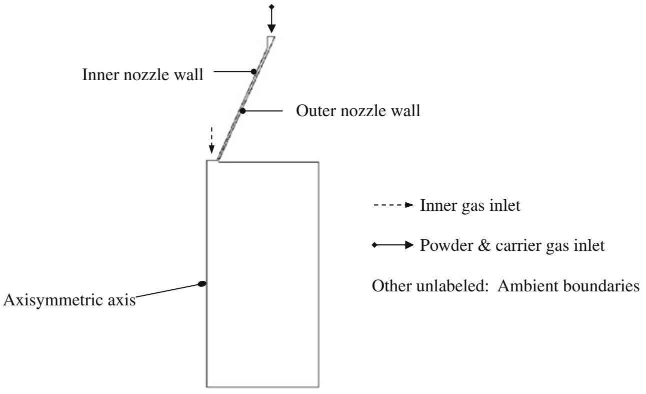

Fig. 2. Schematic calculation domain.

2.4. Governing equations and boundary conditions

2.4.1. Gas turbulent flow

Since the gas–powder flow is characterized by the turbulence [1–8], a turbulent model has been set up to solve the momentum and turbulence equations of the gas phase (argon in this study), and to calculate the particle motions based on the gas flow field. For an axisymmetric, steady, and turbulent continuous gas flow with homogeneous chemical composition and no body force or swirl velocity, the governing equations are given as follows [24,25]:

Continuity equation of mass:

$$\frac{\partial(\rho u_x)}{\partial x}+\frac{1}{r}\frac{\partial}{\partial r}(r\rho u_r)=0 \tag{1}$$

where x and r are, respectively, the axial and radial coordinate, u_x is the axial velocity, u_r is the radial velocity, and ρ is the density of the continuous gas.

The axial momentum conservation equation:

$$\begin{aligned}\frac{\partial(\rho u_x u_x)}{\partial x}+\frac{1}{r}\frac{\partial(r\rho u_r u_x)}{\partial r}=&-\frac{\partial p}{\partial x}+\frac{1}{r}\frac{\partial}{\partial x}\left[r\mu\left(2\frac{\partial u_x}{\partial x}-\frac{2}{3}(\nabla\cdot\vec{u})\right)\right]\\&+\frac{1}{r}\frac{\partial}{\partial r}\left[r\mu\left(\frac{\partial u_x}{\partial r}+\frac{\partial u_r}{\partial x}\right)\right]+\phi_x\end{aligned} \tag{2}$$

The radial momentum conservation equation:

$$\begin{aligned}\frac{\partial(\rho u_x u_r)}{\partial x}+\frac{1}{r}\frac{\partial(r\rho u_r u_r)}{\partial r}=&-\frac{\partial p}{\partial r}+\frac{\partial}{\partial x}\left[\mu\left(\frac{\partial u_x}{\partial r}+\frac{\partial u_r}{\partial x}\right)\right]+\frac{1}{r}\\&\times\frac{\partial}{\partial r}\left[r\mu\left(2\frac{\partial u_r}{\partial r}-\frac{2}{3}(\nabla\cdot\vec{u})\right)\right]\\&-2\mu\frac{u_r}{r^2}+\frac{2}{3}\frac{\mu}{r}(\nabla\cdot\vec{u})+\phi_r\end{aligned} \tag{3}$$

where

$$\nabla\cdot\vec{u}=\frac{\partial u_x}{\partial x}+\frac{\partial u_r}{\partial r}+\frac{u_r}{r} \tag{4}$$

and μ is the effective dynamic viscosity of the continuous gas. $\varphi_i(i=x,\ r)$ is the source term, which herein represents the coupled momentum transport from the particle phase:

$$\phi_i=\frac{1}{V_C}\sum_{j=1}^{n_C}\frac{3\mu C_D Re}{4\rho_p d_p^2}(u_{p,i}-u_i)\dot{m}_p^j\Delta t^j \tag{5}$$

where $\dot{m}_p^j$ is the particle mass rate for the jth trajectory passing through a cell C; V_C is the volume of the cell; $\Delta t^j$is the time that a particle on the jth trajectory takes to pass through the cell; n_C is the total number of particle trajectories passing through the cell; Re and C_D are Reynolds number and the drag coefficient of a particle expressed in Eqs. (14) and (15); ρ_p, d_p, and $u_{p,i}$ are the density, diameter, and velocity in i direction of a particle, respectively.

Since it is a turbulence flow, characterized by fluctuating velocities, extra equations are needed to solve the above ones in a time-averaged manner. So far, the most popular turbulent model is the two-equation model, or k–ε model proposed by Launder and Spalding [26], which describes the turbulence behavior by introducing two additional variables, the turbulent kinetic energy k, and the viscous dissipation rate of turbulent kinetic energy ε. These two equations are expressed as [24]:

Conservation of the kinetic energy of turbulence:

$$\frac{\partial(\rho u_x k)}{\partial x}+\frac{1}{r}\frac{\partial(r\rho u_r k)}{\partial r}=\frac{\partial}{\partial x}\left[\left(\mu_l+\frac{\mu_t}{\sigma_k}\right)\frac{\partial k}{\partial x}\right]+\frac{1}{r}\times\frac{\partial}{\partial r}\left[r\left(\mu_l+\frac{\mu_t}{\sigma_k}\right)\frac{\partial k}{\partial r}\right]+G_k-\rho\varepsilon \tag{6}$$

Conservation of the dissipation of kinetic energy of turbulence:

$$\frac{\partial(\rho u_x\varepsilon)}{\partial x}+\frac{1}{r}\frac{\partial(r\rho u_r\varepsilon)}{\partial r}=\frac{\partial}{\partial x}\left[\left(\mu_l+\frac{\mu_t}{\sigma_\varepsilon}\right)\frac{\partial\varepsilon}{\partial x}\right]+\frac{1}{r}\frac{\partial}{\partial r}\left[r\left(\mu_l+\frac{\mu_t}{\sigma_\varepsilon}\right)\frac{\partial\varepsilon}{\partial r}\right]+C_1G_k\frac{\varepsilon}{k}-C_2\rho\frac{\varepsilon^2}{k} \tag{7}$$

$$G_k=\mu_t\left\{2\left[\left(\frac{\partial u_x}{\partial x}\right)^2+\left(\frac{\partial u_r}{\partial r}\right)^2+\left(\frac{u_r}{r}\right)^2\right]+\left(\frac{\partial u_x}{\partial r}+\frac{\partial u_r}{\partial x}\right)^2\right\} \tag{8}$$

where μ_l and μ_t are laminar and turbulent viscosity, respectively, ($\mu=\mu_l+\mu_t$),$\mu_t=\rho C_\mu k^2/\varepsilon$, and G_k represents the rate of production of kinetic energy. The above equations contain four empirical constants, which are selected as follows [26]: $C_1=1.44$, $C_2=1.92$, $C_\mu=0.09$, $\sigma_k=1.0$, and $\sigma_\varepsilon=1.30$. The commercial computational fluid dynamics (CFD) code, FLUENT, is used to solve the set of equations presented in Eqs. (1)–(8).

2.4.2. Modeling particle flow

The powder used is Stellite 6, a wear resistant alloy, whose physical and thermal properties are shown in Table 1. The size distribution of the powder is displayed by the sieve analysis in Table 2. To describe the size distribution of particles, Rosin–Rammler distribution, frequently used for representing particle/droplet size distribution in sprays, was used. Basically, this approach is to divide the whole range of particle sizes into an adequate number of discrete intervals, with each represented by a mean diameter d for which trajectory calculations will be conducted. According to Rosin–Rammler distribution, the mass fraction of droplets with the diameter greater than d is expressed by Eq. (9) [25],

$$F_d=\exp(-(d/\bar{d})^n) \tag{9}$$

where $\bar{d}$ is the size constant and n is the size distribution parameter (spread parameter). Both of these two parameters need to be determined. Based on the sieve analysis in Table 2, the particles can be classified into different size ranges with different mass fractions in each range as shown in Table 3. The curve fit of the data in Table 3 allows one to determine the size constant $\bar{d}$, which is the d value at $F_d=e^{-1}\approx 0.368$ and turned out to be 96 μm. In Eq. (9), the spread parameter n can be rewritten:

$$n=\frac{\ln(-\ln F_d)}{\ln(d/\bar{d})} \tag{10}$$

By substituting the given data pairs in Table 3 for F_d and $d/\bar{d}$ into Eq. (10) and taking an average, the spread parameter n of 4.23 was obtained. For the powder used in this study, the minimum and maximum diameters were chosen to be 45 and 150 μm, respectively, because particles beyond this range are in very low percentage ($\leqslant$1%). The number of diameters is chosen to be same as the number of diameter ranges shown in Table 2. All the size distribution parameters are summarized in Table 4.

Table 1
Physical and thermal properties of Stellite 6 powder.

Density, ρ_p (kg/m^3)	8380
Specific heat, c_p (J/kg/K)	421
Thermal conductivity, k_p (W/mK)	14.82
Latent heat, L_f (J/kg)	2.92×10^5
Liquidus temperature, T_{liq} (K)	1630
Solidus temperature, T_{sol} (K)	1533

Another practical issue is that the shape of the particles is not exactly spherical [6,7], as can be seen from Fig. 3. It can be noticed that particles are not perfectly spherical but some satellite spheres are attached, which often happens to fine powders during an inert gas atomization process if a small cold particle hits a hot near solidified droplet [27]. Therefore it is necessary to consider the shape effect of the particles in terms of shape factor φ, which is used to describe how spherical a particle is and expressed as [25,28],

$$\varphi=\frac{s}{S} \tag{11}$$

where s is the surface area of a sphere having the same volume as the particle, and S is the actual surface area of the particle. The shape factor is one for a spherical particle, while always less than one for non-spherical particles.

The dynamic governing equations for each particle are represented by [25],

$$\frac{d\vec{x}}{dt}=u_p \tag{12}$$

$$\frac{du_p}{dt}=\frac{18\mu}{\rho_p d_p^2}\frac{C_D Re}{24}(u-u_p)+\frac{g(\rho_p-\rho)}{\rho_p} \tag{13}$$

$$Re=\frac{\rho d_p|u-u_p|}{\mu} \tag{14}$$

where ρ_p, d_p, u_p are the density, diameter, and velocity of each particle, respectively. Basically the particles are driven by the main forces of both gas flow drag and gravity. The drag coefficient expression with the four coefficients accounting for non-spherical particles are written as [25,28]:

$$C_D=\frac{24}{Re}(1+a_1Re^{a_2})+\frac{a_3Re}{a_4+Re} \tag{15}$$

$$\begin{aligned}a_1&=\exp(2.3288-6.4581\varphi+2.4486\varphi^2)\\a_2&=0.0964+0.5565\varphi\\a_3&=\exp(4.905-13.8944\varphi+18.4222\varphi^2-10.2599\varphi^3)\\a_4&=\exp(1.4681+12.2584\varphi-20.7322\varphi^2+15.8855\varphi^3)\end{aligned} \tag{16}$$

Based upon the pictures shown in Fig. 3, a value of 0.8 is chosen as the shape factor for the satelliting shape particles [5].

Since the gas flow is turbulence, it is necessary to determine if the particles are heavy enough not to be influenced by the fluctuating velocities of the gases. This effect can be checked by the Stokes number, a very important parameter in fluid-particle flows [29], which measures if the particle has enough time to respond to the instant changes in flow velocity. The Stokes number related to the particle velocity is defined as [29]:

$$St=\frac{\tau_p}{\tau} \tag{17}$$

in which τ_p is the velocity response time of the particles and τ is some time characteristic of the gas flow. A practical expression of the particle's Stokes number is given by [30]:

$$St=\frac{1}{18}\gamma_d^2\gamma_\rho Re \tag{18}$$

where $\gamma_d=d_p/D$, $\gamma_\rho=\rho_p/\rho$, Re is the Reynolds number, and D is some characteristic dimension of the powder flow and was chosen to be the channel width of the powder passage. After entering the values

Table 2
Sieve analysis of Stellite 6 powder.

Sieve type	80 mesh	100 mesh	140 mesh	200 mesh	270 mesh	325 mesh	Pan
Size (μm)	(>180)	(150–180)	(106–150)	(75–106)	(53–75)	(45–53)	(<45)
Results (%)	0.0	1.0	25.4	36.5	32.7	3.8	0.7

Table 3
Mass fraction in particle diameter range.

Diameter, d (μm)	Mass fraction with diameter greater than d, F_d (%)
45	99.3
53	95.5
75	62.8
106	26.3
150	1.0
180	0.0

Table 4
Summary of powder size distribution parameters.

Minimum diameter (μm)	45
Maximum diameter (μm)	150
Mean diameter (μm)	96
Number of diameters (#)	6
Spread parameter	4.23

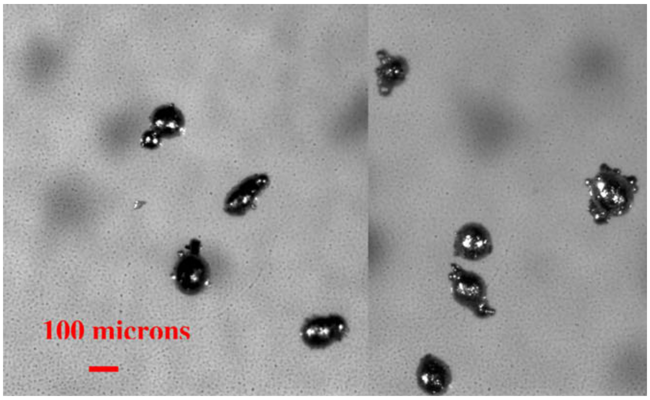

Fig. 3. Non-spherical (Satelliting) particles.

of the given parameters into Eq. (17), a rough calculation showed that for the powder flow conditions of the present study, the value of St is much larger than 1. Therefore it indicates that the particles are heavy enough such that they do not respond to the fluctuation of the gas velocities, which means the gas velocities in Eqs. (12)–(14) are time-averaged ones.

Within the nozzle, each particle is assumed to retain its normal and tangential momentums. Another assumption is that there is no collision between each two particles, which is based on the fact that the powder feed rate is very small such that the possibility of two particles collision is very low. In this study, the Lagrangian approach of the discrete phase model (DPM) in FLUENT has been used to solve each particle's dynamic behavior described by Eqs. (12)–(16).

2.4.3. Modeling particle heating process

During the flight of particles, they will travel through the laser irradiation zone where the particles are heated up by the laser. This thermal behavior is important since it determines how much additional thermal energy the particles will bring when hitting the melt pool. Although the particle melting process with constant melting temperature has been modeled [13–15,19–22], there have been very few studies reported on liquid fraction evolution during the alloy material particle heating process. This paper presents a model that is capable of modeling liquid fraction evolution for the alloy particles during the phase change under laser irradiation.

To consider the process of phase change for a particle, an energy equation is proposed as follows:

$$m_p c_p \frac{dT_p}{dt} = hA_p(T_\infty - T_p) + \xi I \frac{A_p}{4} - m_p L_f \frac{df}{dt} \tag{19}$$

where m_p is the total mass of a particle, c_p is the specific heat capacity, A_p is the particle surface area, $A_p/4$ denotes the effective projection area of a particle visible by the beam, and T_p and T_∞ are the temperatures of the particle and surrounding gas, respectively, I is the laser intensity on the particles, ξ is the particle absorptivity of laser power, which is assumed to be constant, and L_f is the latent heat of the particle material. h is the convection coefficient, which is determined from Nusselt number [31,32]:

$$Nu = \frac{hd_p}{\lambda} = 2 + 0.6Re^{0.5}Pr^{0.33} \tag{20}$$

where λ is the thermal conductivity of the surrounding gases, and $Pr(= c_p\mu/\lambda)$ is the Prandtl number. f is the liquid fraction, which is expressed as:

$$f = \frac{m_l}{m_p} = \begin{cases} 0 & T_p \leqslant T_{sol} \\ \frac{T_p - T_{sol}}{T_{liq} - T_{sol}} & T_{sol} < T_p < T_{liq}\ (0 \le f \le 1) \\ 1 & T_p \ge T_{liq} \end{cases} \tag{21}$$

where T_{sol} and T_{liq} are, respectively, solidus and liquidus temperatures for the alloy particles. For Stellite 6 powder used in this study, an absorptivity of 0.47 for Nd:YAG laser [33,34] was taken. m_l is the mass of liquid part of a particle during its phase change. Within the phase change, f is increased from 0 to 1, that is, from completely solid to totally liquid. Basically, how the particle temperature evolves is dominated by the laser heating, ambient gas convection and latent heat of its phase change rate as indicated by Eq. (19).

From Eq. (21), one can obtain

$$\frac{df}{dt} = \begin{cases} \left(\frac{1}{T_{liq} - T_{sol}}\right)\frac{dT_p}{dt} & T_{sol} < T_p < T_{liq} \\ 0 & T_p \leqslant T_{sol} \quad \text{or} \quad T_p \ge T_{liq} \end{cases} \tag{22}$$

Substituting Eq. (22) into (19) yields

$$\left(m_p c_p + \frac{\delta m_p L_f}{T_{liq} - T_{sol}}\right)\frac{dT_p}{dt} = hA_p(T_\infty - T_p) + \xi I \frac{A_p}{4} \tag{23}$$

$$\delta = \begin{cases} 1 & T_{sol} < T_p < T_{liq} \\ 0 & T_p \le T_{sol}\, \text{or}\, T_p \ge T_{liq} \end{cases} \tag{24}$$

which can be rewritten as

$$\frac{d(T_p - \alpha_p)}{dt} = -\beta_p(T_p - \alpha_p) \tag{25}$$

where

$$\begin{cases} \alpha_p = T_\infty + \frac{\xi I}{4h} \\ \beta_p = \frac{hA_p}{m_p c_p + \frac{\delta m_p L_f}{T_{liq} - T_{sol}}} \end{cases} \tag{26}$$

Integrating Eq. (25) from t to $t + \Delta t$ yields

$$\int_{T_p(t)}^{T_p(t+\Delta t)} \frac{d(T_p-\alpha_p)}{T_p-\alpha_p} = \int_t^{t+\Delta t} -\beta_p dt \tag{27}$$

The iteration form of particle temperature finally becomes

$$T_p^{i+1} = \alpha_p + (T_p^i - \alpha_p)\exp(-\beta_p \Delta t) \tag{28}$$

where T_p^i denotes the particle temperature at time step level i with Δt as the time step value, which is very small ($\sim 10^{-5}$ s) so that laser intensity varies little during each time step. This particular algorithm has been incorporated into FLUENT as a user defined function to calculate the particle temperature evolution in the powder stream along with the simulation of Lagrangian particle dynamic model discussed in Section 2.4.2.

Since the laser beam is Gaussian, the following equation has been used to describe the distribution of the laser intensity:

$$I(x,r) = \frac{2P}{\pi R_b^2(x)} \exp\left[-2\frac{r^2}{R_b^2(x)}\right] \tag{29}$$

in which R_b is the effective radius (0.75 mm) of the laser beam and P is the laser power. The laser intensity profile and its position with respect to the nozzle are shown in Fig. 4 for $P = 300$ W. The laser beam converges with a half angle of 3.7° to the focal point at $x \approx 8.5$ mm, followed by a 5 mm DOF (depth of field), and then diverges by the same angle. The center black line in Fig. 4 is due to the mirror stitching of the two calculation domains. Because of the very small powder feed rate which results in a very dilute powder cloud, the laser power attenuation effect was neglected. This assumption is reasonable according to the research in [35,36].

The laser intensity value defined in Eq. (29) is numerically stored in the user-defined memory [37] of a local cell. In this way, the spatial laser intensity field value can be assigned to each cell in the calculation domain. As calculation continues, the simulation of the particle heating process is accomplished via the iteration form in Eq. (28) by retrieving the stored value in a cell into the variable I as the particle travels through the cell.

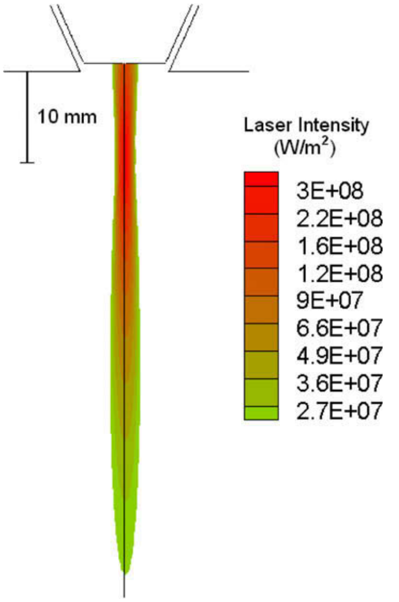

Fig. 4. Laser intensity profile. Laser power, 300 W; beam radius, 0.75 mm.

3. Results and discussion

3.1. Powder stream structure

The operating parameters have been set such that the powder feeding rate was 3 g/min with 7.86×10^{-5} m^3/s (10 SCFH) of shielding (inner) gas and 7.86×10^{-5} m^3/s (10 SCFH) of carrier gas. Fig. 5 depicts the simulated powder stream structure formed by multi-particle trajectories. It can be seen that the powder stream begins to expand at the exit of the nozzle. Such expansion is due to gravity and the mixed flow field of inner and carrier gases. The particle streams merge into a main stream to form a waist, at the distance of around 9 mm below the nozzle tip. After traveling further distance, the main stream diverges, because the particles flow in different directions naturally. According to the characteristics of the powder stream structure, the powder flow below the nozzle may be approximately categorized into three distinct stages, pre-waist, waist, and post-waist, which are labeled by (a–c), respectively, in Fig. 5. To get the detailed information about each stage, three particle concentration plots of nine different planes below the nozzle are shown in Fig. 6.

As seen in Fig. 6(a), before stream convergence, the particles' peak concentration increases as x increases and the position of the peak value is shifting towards the center, which indicates that the particle stream is converging but not yet converged. After particles' merging (approximately at $x \approx 9.0$ mm), the concentration on the centerline first increases to the maximum at around $x \approx 12.0$ mm and then decreases. The waist is about 2 mm in diameter as can be seen from Fig. 6(b). The waist stage ends approximately at $x = 18$ mm. In the post-waist stage, the peak concentration at the center decreases fast and eventually the powder stream diverges.

It is worth to note that this distinct three-stage powder stream structure of the present study is different from the typical ones,

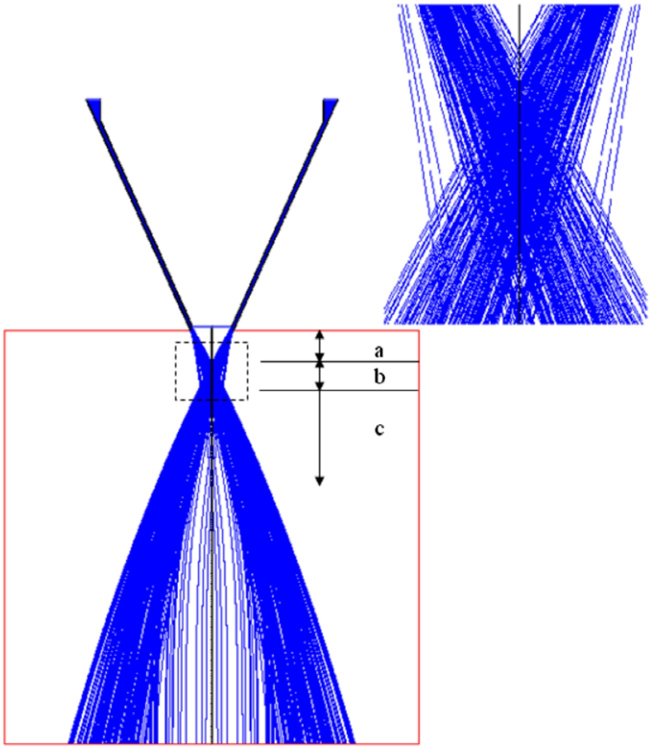

Fig. 5. Particle stream structure: (a) pre-waist stage; (b) waist stage; (c) post-waist stage. Powder flow rate, 3 g/min; inner gas flow rate, 7.86×10^{-5} m^3/s; carrier gas flow rate, 7.86×10^{-5} m^3/s.

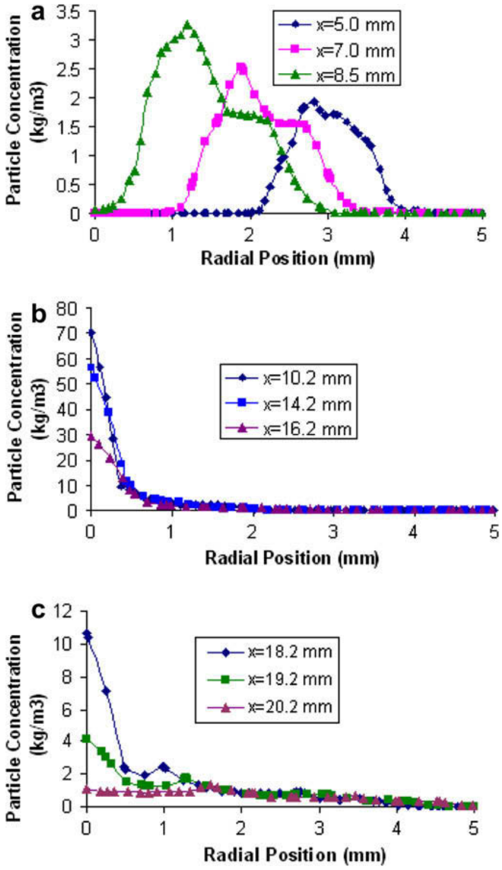

Fig. 6. Particle concentration profiles of the three distinct stages for coaxial powder stream: (a) pre-waist stage; (b) waist stage; (c) post-waist stage. Powder flow rate, 3 g/min; 7.86×10^{-5} m^3/s; carrier gas flow rate, 7.86×10^{-5} m^3/s.

which were characterized by a convergence of powder streams to a point of maximum concentration, followed by a single expanding stream with a Gaussian powder concentration profile [1–7]. The difference may be due to the different coaxial nozzle configurations. For the nozzle used in this study, it has no outer gas, and therefore the powder flow is not restricted by the outer gas that may keep the powder jet from diverging after its convergence in those coaxial nozzles. The predicted powder stream structure has been validated by the experimental measurement, and a reasonable match can be seen from Fig. 7.

3.2. Deposition zone prediction

The deposition zone can be predicted at the same time according to the local particle concentration and laser intensity distribution, the combination of which depends on the user requirements. In this paper, the desirable deposition zone, which was chosen to be the overlap zone of the powder stream waist and the depth of field of the focused laser beam, has been predicted and displayed to be in the range of $x \approx 10$–14 mm as shown in Fig. 8.

3.3. Powder stream temperature distribution

In addition to the powder stream structure, another important issue is the powder heating process. The powder temperature profile has been predicted as in Fig. 9. As seen in Fig. 9, indicated by the steep color transition, the particles experience a sharp increase of temperature at the moment they enter the laser particle interaction zone. The particles are quickly heated up from ambient temperature to around 1000 K or even higher when passing through the laser irradiation zone. It is worth to note that the particle trajectory is critical to determining the particle temperature history because it determines the laser particle interaction time and the laser intensity that the particle experiences, thus influencing the powder temperature distribution. Since each particle trajectory may be different, the heating-up process for multi-particles is complex. To reveal the detailed thermal behavior of multi-particles in the particle stream, three planes at different x positions have been selected to study the particle temperature distributions, which are displayed in Fig. 10. As seen in Fig. 10(a) at $x = 10$ mm, the temperatures of the particles at the center are the highest and decay in the radial direction. However this temperature distribution changes

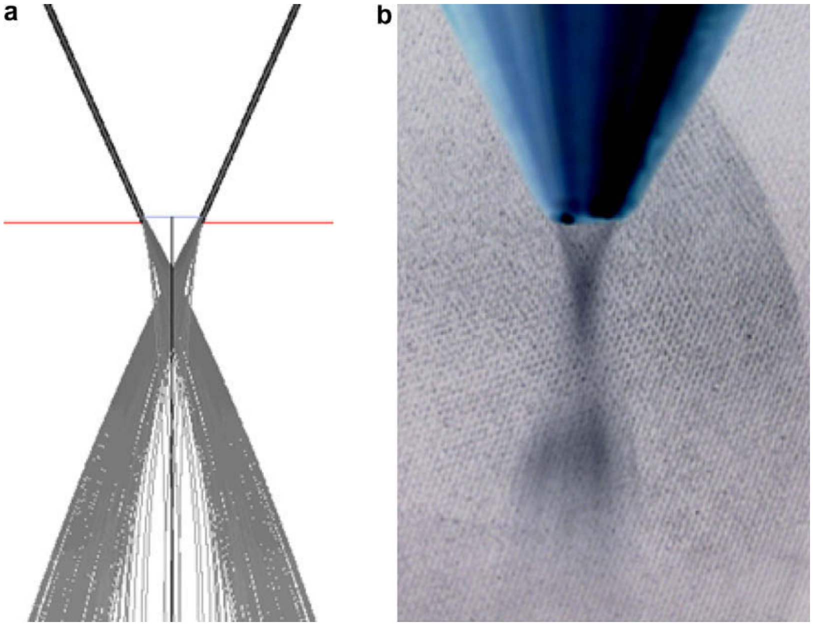

Fig. 7. Validation of the predicted powder stream structure: (a) predicted (cross-section view); (b) experimental (front view). Powder flow rate, 3 g/min; inner gas flow rate, 7.86×10^{-5} m^3/s, carrier gas flow rate, 7.86×10^{-5} m^3/s.

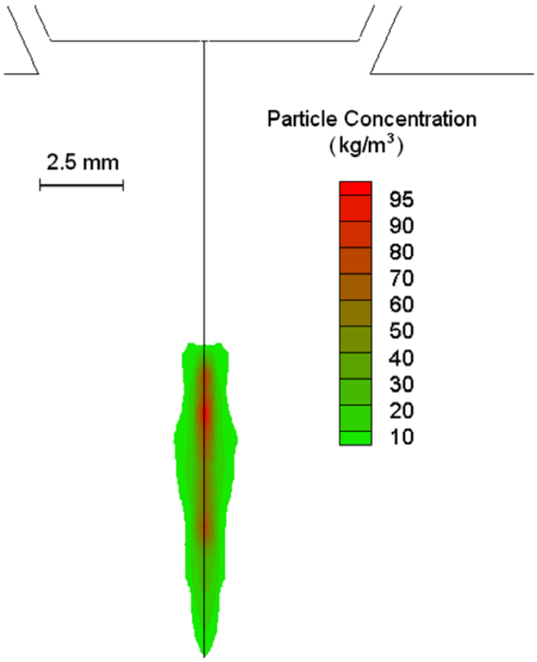

Fig. 8. Desirable deposition zone predictions ($x1 = 10$ mm, $x2 = 14$ mm). Laser power, 300 W; beam diameter, 1.5 mm; powder flow rate, 3 g/min; inner gas flow rate, 7.86×10^{-5} m^3/s, carrier gas flow rate, 7.86×10^{-5} m^3/s.

when the plane moves down as seen in Fig. 10(b) and (c). The temperatures of powders become bi-modal within a radial distance of about 1.5 mm.

An important mechanism explaining the above interesting phenomenon may be schematically illustrated in Fig. 11. In Fig. 11, the range of the laser beam is represented by the dashed red lines. As seen in Fig. 10(a), the plane of $x = 10$ mm is located where particles have just converged. Therefore the particles falling on some point of the plane are mostly from one sub-stream whose heating length is indicated by the green part of the particle trajectory. It is evident that the particles that travel to the points closer to the center are subject to a longer laser irradiation time along with higher laser intensity. This explains the trend that the particle temperature is high at the center while deceasing in the radial direction as in Fig. 10(a). However, in Fig. 11(b), the plane of $x = 14$ mm is located at some distance below the converging point. The particles falling on this plane have another source, that is, the mirror sub-stream. Both the streams are contributing to the particle temperatures at some point as indicated in Fig. 11(b). As seen in Fig. 11(b), the laser heating lengths are different, and hence particle temperatures become bi-modal as shown in Fig. 10(b) and (c). It can be expected that after the stream totally diverges, the particle temperature distribution will become single-modal again. This bi-modal characteristic was also noted earlier by Pinkerton [16].

3.4. Experimental validation

An experiment was carried out to validate the calculated results. The experimental setup is schematically shown in Fig. 12, where a thermal camera (SprayWatch-2i, temperature measurement range 1000–4000 °C) was used to measure the powder flow. The SprayWatch camera detects particle traces and particle temperatures. The particle velocity is measured by dividing the length of trace with the known camera shutter time. Temperatures of the particles are measured by two-color pyrometry [38]. The powder material was Stellite 6.

Before the experiment, a ruler was placed underneath the nozzle tip along the center axis of the nozzle. The SprayWatch camera was adjusted to focus on the ruler so that a sharp image could be obtained in the actual measurement. Thus the center position of the image could be determined based on the ruler scale. As depicted in Fig. 12, the SprayWatch camera was placed on a stage, the height of which could be adjusted to obtain a desired height position. During the experiment, when the powder flow rate became stable, measurement of the powder flow heated by the laser beam was taken by the SprayWatch and its software processed the particles' information and automatically stored measured average

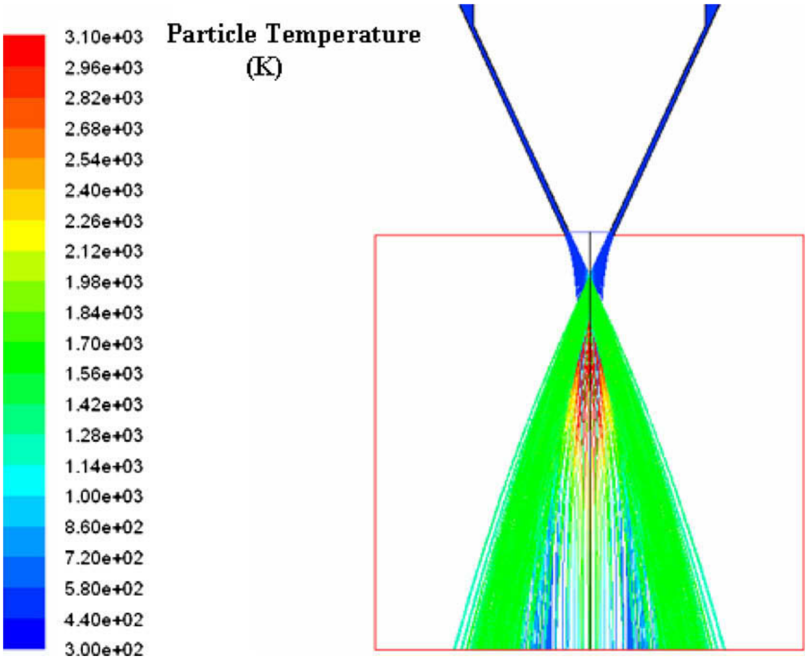

Fig. 9. Powder jet temperature profile. Laser power, 300 W; beam diameter, 1.5 mm; powder flow rate, 5 g/min; inner gas flow rate, 7.86×10^{-5} m^3/s, carrier gas flow rate, 7.86×10^{-5} m^3/s.

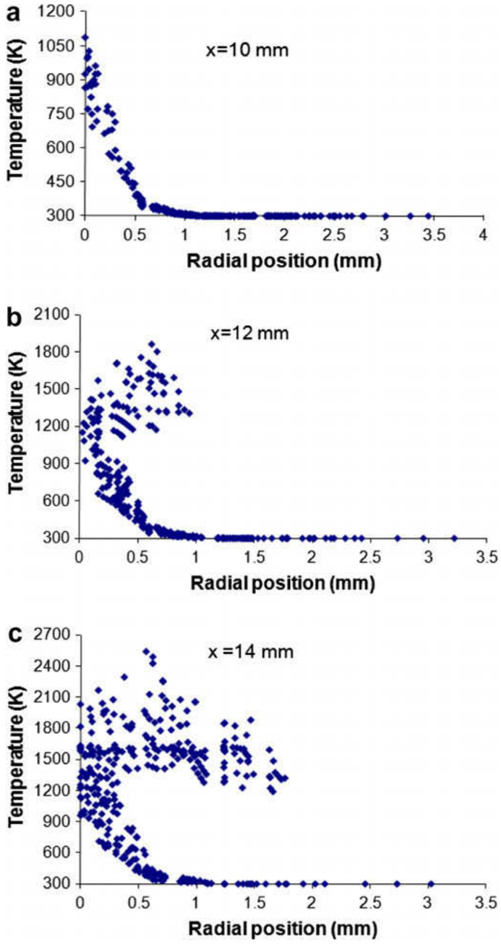

Fig. 10. Powder temperature distribution at different planes: (a) $x = 10$ mm; (b) $x = 12$ mm; (c) $x = 14$ mm. Laser power, 300 W; beam diameter, 1.5 mm; powder flow rate, 5 g/min; inner gas flow rate, 7.86×10^{-5} m^3/s; carrier gas flow rate, 7.86×10^{-5} m^3/s.

velocity and temperature data in the log file [39]. Three distances were chosen for the measurement: 22.5, 32.5, and 42.5 mm away from the nozzle tip. At each distance, the recorded data were averaged over time so that a steady-state value could be obtained.

Fig. 13 shows an example of predicted distributed particle temperature and velocity data in the measurement window at 22.5 mm distance. Note that the temperature distribution in Fig. 13 looks different than those in Fig. 10, mainly because at 22.5 mm distance, the powder stream almost totally diverges,

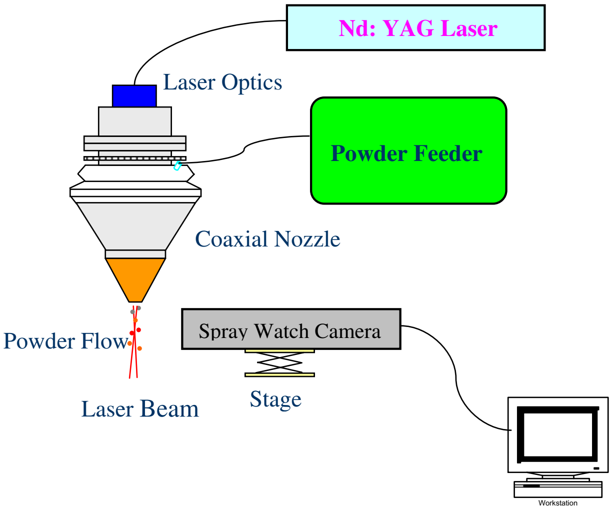

Fig. 12. Experimental setup for powder velocity and temperature measurement.

resulting in a transition from the bi-modal powder temperature distribution to a single-modal distribution again. A small amount of particles whose temperatures are above the evaporating temperature 2800 °C [14] are considered evaporated and not plotted. The corresponding average temperature and velocity values with variations at the three distances are plotted with experimental data in Figs. 14 and 15, respectively. The predicted average values agree with the experimental data well.

The average powder temperature decreases from 1800 to 1500 K as the distance increases from 22.5 to 42.5 mm, which is due to the convection effect. The powder velocity is around 1.15 m/s. Although the experimental velocities do not show a clear trend, the simulated velocity decreases slightly when the distance increases. This is due to the loss of the driving force as the gas expands beneath the nozzle tip and becomes slower further away from the nozzle.

4. Conclusions

A systematic model that describes the dynamic and thermal behavior of the coaxial powder flow for direct deposition processes has been presented. Predicted particle temperatures and velocities have been verified by experimental results. By solving the coupled momentum transfer equations between the particle and gas phase while incorporating a unique subroutine for particle temperature evolution, the dynamic and thermal behavior of multi-particles

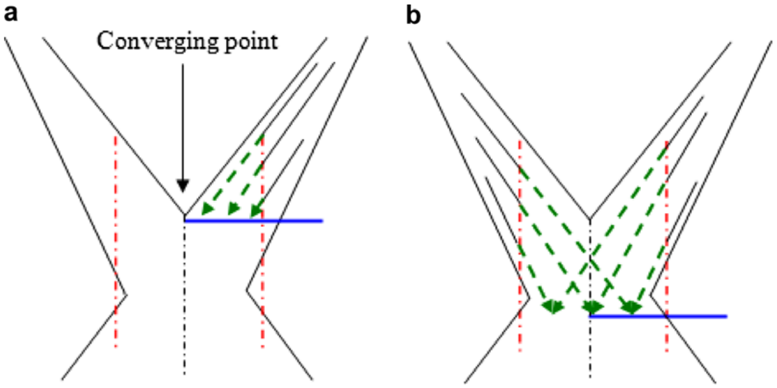

Fig. 11. Schematic of the mechanism for particle temperature distribution at different planes: (a) $x = 10$ mm; (b) $x = 14$ mm.

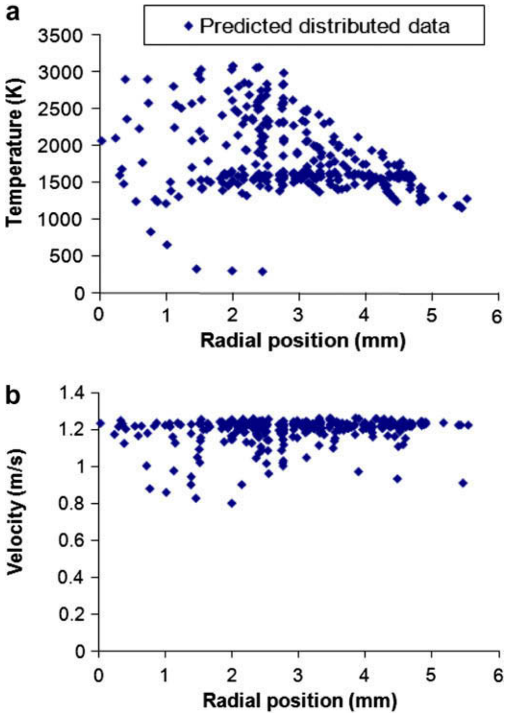

Fig. 13. Calculated particle (a) temperature and (b) velocity distribution values at distance $x = 22.5$ mm away from the nozzle tip. Laser power, 300 W; beam diameter, 1.5 mm; powder flow rate, 5 g/min; inner gas flow rate, 7.86×10^{-5} m^3/s; carrier gas flow rate, 7.86×10^{-5} m^3/s.

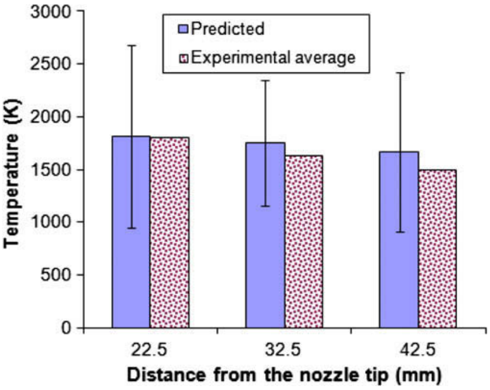

Fig. 14. Comparison between the experimental and calculated particle temperatures at distances of 22.5, 32.5, and 42.5 mm away from the nozzle tip. Laser power, 300 W; beam diameter, 1.5 mm; powder flow rate, 5 g/min; inner gas flow rate, 7.86×10^{-5} m^3/s; carrier gas flow rate, 7.86×10^{-5} m^3/s.

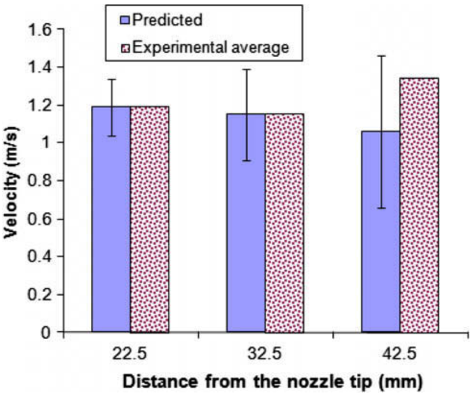

Fig. 15. Comparison between the experimental and calculated particle velocities at distances of 22.5, 32.5, and 42.5 mm away from the nozzle tip. Laser power, 300 W; beam diameter, 1.5 mm; powder flow rate, 5 g/min; inner gas flow rate, 7.86×10^{-5} m^3/s; carrier gas flow rate, 7.86×10^{-5} m^3/s.

in the stream has been completely modeled. The modeling results show that the coaxial powder jet may be categorized into three distinct stages: pre-waist, waist, and post-waist, with different particle concentrations for each. According to the combination of powder concentration and laser beam conditions, a desirable deposition zone was predicted, thus offering an approach to the selection of a desirable deposition plane for laser direct deposition. In addition, the laser heating process of alloy particles has been modeled and the multi-particle temperature distribution at different deposition planes has been revealed. It has been shown that at the plane very close to the jet converging point, the particle temperature is high in the center and deceases in the radial direction, while in those planes below the converging point, it becomes bi-modal. After the powder stream totally diverges, its temperature distribution becomes single-modal again. The underlying mechanism has been explained based on particle trajectories and consequent laser-interacting lengths at different planes. The model is capable of predicting the powder stream structure and multi-particle phase change process with liquid fraction evolution for various coaxial nozzle designs while considering the particle morphology and size distribution in real powder samples. Therefore, the presented model can be used to optimize powder flow conditions, thus helping controlling direct deposition processes.

Acknowledgments

The authors gratefully acknowledge the financial support provided for this study by the National Science Foundation (Grant Nos: IIP-0538786 and IIP-0917936) and State of Indiana through the 21st Century R&T Fund.

References

[1] N. Yang, Concentration model based on movement model of powder flow in coaxial laser cladding, Opt. Laser Technol. 41 (1) (2009) 94–98.
[2] J. Lin, Concentration mode of the powder stream in coaxial laser cladding, Opt. Laser Technol. 31 (3) (1999) 251–257.
[3] J. Lin, Numerical simulation of the focused powder streams in coaxial laser cladding, J. Mater. Process. Technol. 105 (1) (2000) 17–23.
[4] H. Pan, F. Liou, Numerical simulation of metallic powder flow in a coaxial nozzle for the laser aided deposition process, J. Mater. Process. Technol. 168 (2) (2005) 230–244.
[5] H. Pan, T. Sparks, Y.D. Thakar, F. Liou, The investigation of gravity driven metal powder flow in coaxial nozzle for laser-aided direct metal deposition process, Trans. ASME J. Manuf. Sci. Eng. 128 (2) (2006) 541–553.
[6] A.J. Pinkerton, L. Li, A verified model of the axial powder stream concentration from a coaxial laser cladding nozzle, in: Proceedings of International Congress on Applications of Lasers and Electro-optics (ICALEO'02), Scottsdale, Arizona, U19SA CD, 2002.
[7] A.J. Pinkerton, L. Li, Modelling powder concentration distribution from a coaxial deposition nozzle for laser-based rapid tooling, Trans. ASME J. Manuf. Sci. Eng. 126 (1) (2004) 33–41.
[8] A.J. Pinkerton, L. Li, The development of temperature fields and powder flow during laser direct metal deposition wall growth, J. Mech. Eng. Sci. 218 (2004) 531–541.
[9] S. Zekovic, R. Dwivedi, R. Kovacevic, Numerical simulation and experimental investigation of gas-powder flow from radially symmetrical nozzles in laser-based direct metal deposition, Int. J. Mach. Tools Manuf. 47 (2007) 112–123.
[10] J.C. Liu, L.J. Li, X.Z. Xie, X.Z. Jin, J.G. Lu, Study on attenuation of laser power by powder flow in coaxial laser cladding, in: Proceedings of SPIE – The International Society for Optical Engineering, Lasers in Mater. Process. Manuf. II, vol. 5629, 2005, pp. 475–482.
[11] J.C. Liu, L.J. Li, Y.Z. Zhang, X.Z. Xie, Attenuation of laser power of a focused gaussian beam during interaction between a laser and powder in coaxial laser cladding, J. Phys. D Appl. Phys. 38 (10) (2005) 1546–1550.
[12] M. Grujicic, Y. Hu, G.M. Fadel, D.M. Keicher, Optimization of the LENS rapid fabrication process for in-flight melting of feed powder, J. Mater. Synth. Process. 9 (5) (2001) 223–233.

[13] J. Lin, Temperature analysis of the powder streams in coaxial laser cladding, Opt. Laser Technol. 31 (8) (1999) 565–570.

[14] C.Y. Liu, J. Lin, Thermal processes of a powder particle in coaxial laser cladding, Opt. Laser Technol. 35 (2) (2003) 81–86.

[15] P.A. Vetter, T. Engel, J. Fontaine, Laser cladding: the relevant parameters for process control, in: Proceedings of SPIE 2207, 1994, pp. 452–462.

[16] A.J. Pinkerton, An analytical model of beam attenuation and powder heating during coaxial laser direct metal deposition, J. Phys. D Appl. Phys. 40 (2007) 7323–7334.

[17] Y.C. Fu, A. Loredo, B. Martin, A.B. Vannes, A theoretical model for laser and powder particles interaction during laser cladding, J. Mater. Process. Technol. 128 (2002) 106–112.

[18] Y.L. Huang, G.Y. Liang, J.Y. Su, J.G. Li, Interaction between laser beam and powder stream in the process of laser cladding with powder feeding, Modell. Simul. Mater. Sci. Eng. 13 (2005) 47–56.

[19] O.D.O. Neto, A.M. Alcalde, R. Vilar, Interaction of a focused laser beam and a coaxial powder jet in laser surface processing, J. Laser Appl. 19 (2) (2007) 84–88.

[20] L. Han, F.W. Liou, K.M. Phatak, Modeling of laser cladding with powder injection, Metall. Mater. Trans. B 35B (2004) 1139–1150.

[21] L.J. Han, K.M. Phatak, F.W. Liou, Modeling of laser deposition and repair process, J. Laser Appl. 17 (2) (2005) 89–99.

[22] H. Qi, J. Mazumder, H. Ki, Numerical simulation of heat transfer and fluid flow in coaxial laser cladding process for direct metal deposition, J. Appl. Phys. 100 (2006) 024903.

[23] X. He, J. Mazumder, Transport phenomena during direct metal deposition, J. Appl. Phys. 101 (2007) 053113.

[24] M.A. Serag-Eldin, D.B. Spalding, Computations of three-dimensional gas turbine combustion chamber, J. Eng. Power 101 (1979) 327–336.

[25] Fluent 6.3 User Manual, Fluent Inc. Canonsburg, Pennsylvania, USA, 2006.

[26] B.E. Launder, D.B. Spalding, Lectures in Mathematical Models of Turbulence, Academic Press, London, England, 1972.

[27] J. Dunkley, Anti-satelliting for powders produced by inert gas atomization, Mater. World 10 (7) (2002) 24–25.

[28] A. Haider, O. Levenspiel, Drag coefficient and terminal velocity of spherical and nonspherical particles, Powder Technol. 58 (1989) 63–70.

[29] C. Crowe, M. Sommerfeld, Y. Tsuji, Mutiphase Flows with Droplets and Particles, CRC Press LLC, Florida, USA, 1998.

[30] R.B. Ye, P. Proulx, M.I. Boulos, Particle turbulent dispersion and loading effects in an inductively coupled radio frequency plasma, J. Phys. D Appl. Phys. 33 (2000) 2154–2162.

[31] W.E. Ranz, W.R. Marshall Jr., Evaporation from Drops, Part I, Chem. Eng. Prog. 48 (3) (1952) 141–146.

[32] W.E. Ranz, W.R. Marshall Jr., Evaporation from Drops, Part II, Chem. Eng. Prog. 48 (4) (1952) 173–180.

[33] F. Lemoine, D.F. Grevey, I. Vastra Bobin, A.B. Vannes, Laser cladding cross-section modelling obtained by metallic powder spraying into a Nd:YAG laser beam, J. Phys. III 3 (10) (1993) 2043–2052.

[34] J.M. Jouvard, D.F. Grevey, F. Lemoine, A.B. Vannes, Continuous wave Nd:YAG laser cladding modeling: a physical study of track creation during low power processing, J. Laser Appl. 9 (1997) 43–50.

[35] C. F. Marsden, A. Frenk, J.D. Wagniere, Power absorption during the laser cladding process, in: B.L. Mordike (Ed.), Laser Treatment of Materials, DGM, Oberurel, 1987, pp. 375–380.

[36] M. Picasso, C.F. Marsden, J.D. Wagniere, A. Frenk, M. Rappaz, A simple but realistic model for laser cladding, Metall. Mater. Trans. B 25B (1994) 281–291.

[37] Fluent 6.3 UDF Manual, Fluent Inc. Canonsburg, Pennsylvania, USA, 2006.

[38] Available from: <http://www.oseir.com>, Oseir Ltd., Finland.

[39] SprayWatch-2i standard user manual, Oseir Ltd., Finland.